Marine burial of terrestrial organic carbon modulates past warm climates

Gordon Inglis

Gordon.Inglis@soton.ac.uk

University of Southampton https://orcid.org/0000-0002-0032-4668

Jordon Hemingway

ETH Zurich https://orcid.org/0000-0002-8299-2255

Richard Stockey

University of Southampton https://orcid.org/0000-0001-5541-7987

Emily Hollingsworth

University of Southampton

Paul Valdes

Bristol University https://orcid.org/0000-0002-1902-3283

Alexander Farnsworth

University of Bristol https://orcid.org/0000-0001-5585-5338

Felix Elling

Harvard University https://orcid.org/0000-0003-0405-4033

Marcus Badger

Open University https://orcid.org/0000-0001-8195-5244

Richard Pancost

University of Bristol

Ann Pearson

Harvard University

Thomas Gernon

University of Southampton https://orcid.org/0000-0002-7717-2092

Robert Hilton

University of Oxford https://orcid.org/0000-0002-0499-3332

Article

Keywords:

Posted Date: September 3rd, 2025

DOI: https://doi.org/10.21203/rs.3.rs-7272686/v1

Additional Declarations: There is **NO** Competing Interest.

Marine burial of terrestrial organic carbon modulates past warm climates

Gordon N. Inglis[1], Jordon Hemingway[2], Richard Stockey[1], Emily Hollingsworth[1], Paul Valdes[3,4], Alex Farnsworth[3,4], Felix J. Elling[5], Marcus Badger[6], Richard D. Pancost[7], Ann Pearson[8], Thomas M. Gernon[1], and Robert Hilton[9].

(1) School of Ocean and Earth Science, University of Southampton, UK
(2) Geological Institute, Department of Earth and Planetary Sciences, ETH Zurich, Switzerland
(3) School of Geographical Sciences, University of Bristol, UK
(4) State Key Laboratory of Tibetan Plateau Earth System, Environment and Resources Institute of Tibetan Plateau Research, Chinese Academy of Sciences, Beijing, China.
(5) Leibniz-Laboratory for Radiometric Dating and Isotope Research, Christian-Albrechts-University of Kiel, Kiel, Germany
(6) School of Environment, Earth and Ecosystem Sciences, The Open University, Milton Keynes, UK
(7) Department of Earth Science and School of Chemistry, University of Bristol, UK
(8) Department of Earth and Planetary Sciences, Harvard University, Cambridge, MA, USA
(9) Department of Earth Sciences, University of Oxford, Oxford OX1 3AN, United Kingdom

Corresponding author: Gordon N. Inglis
Email: gordon.inglis@soton.ac.uk. Telephone: +44 (0)117 954 6395

Abstract

The Palaeocene-Eocene Thermal Maximum (PETM), ~56 million years ago, was characterised by large-scale carbon release (~3,000-10,000 petagrams of carbon) and transient global warming (4-6°C over 10,000 years). Erosion and subsequent burial of terrestrial organic carbon (OC) in marine sediments could have sequestered OC during the PETM – stabilising the Earth system – yet direct evidence is lacking. Here we present new source-specific biomarker records from five globally distributed shallow marine sites and show that plant and soil OC contribute ~40-95% of total OC in coastal marine sediments during the PETM. This is higher than modern marine sediments (~12-20% of total OC) and implies greater terrestrial OC burial in marine environments during past warm climates. Terrestrial OC burial fluxes can increase ~10-to-50-fold during the PETM due to enhanced physical erosion and higher coastal sedimentation rates. This implies that marine burial of terrestrial OC modulated climate during the PETM and possibly other hyperthermals. Current models do not account for this expanded delivery of terrestrial OC into the marine realm and are thus missing an important

carbon sink. Terrestrial OC burial could have acted as a negative feedback in warmer-than-present climates and may aid the long-term (>10,000 year) recovery of the Earth system.

Introduction

The geological record is punctuated by transient warming events (hyperthermals) of differing rates and magnitudes [1]. Hyperthermals are characterised by (i) rapid warming with a relatively abrupt onset (1,000 to 10,000 years) followed by an extended duration (>100,000 years); and (ii) input of ^{13}C-depleted carbon into the ocean-atmosphere system, recorded as a negative carbon isotope excursion (CIE). The PETM is the largest hyperthermal of the Cenozoic Era and is characterised by an approximate doubling of atmospheric CO_2 (from ~1,200 to ~2,500 ppm) [2], a negative CIE (ca. -4 ‰) [3], and transient global warming (4-6 °C rise in global temperatures over 10,000 years) [4]. The PETM has provided unique insights into the potential drivers of CO_2 release [5] and how the Earth system responds to geologically rapid warming events [1]. The magnitude of cooling during the termination of the PETM is well constrained [2, 3, 5], but the processes governing the recovery of the climate system during the PETM and other hyperthermals remain unclear.

Over geological timescales, carbon dioxide (CO_2) can be removed from the ocean-atmosphere system via silicate weathering and/or organic carbon (OC) burial [6]. Silicate weathering coupled to carbonate burial is an important atmospheric CO_2 sink over relatively long (>10^5 to 10^6 year) timescales [6]. This mechanism is thought to respond and contribute to major climate transitions during the Phanerozoic [7], acting as a stabilising negative feedback to global warming [8]. Silicate weathering is also important over shorter PETM-relevant timescales (~10^4 years) with a prediction that weathering fluxes increased by ~50-60 % during the PETM relative to pre-event values [9]. This increase has been interpreted to reflect more intense mineral weathering and a shift toward higher physical erosion rates due to changes in hydroclimate [9], both of which are consistent with increased nutrient and clay delivery into coastal environments [10]. Increasing nutrient delivery can stimulate marine primary productivity and enhance marine organic carbon burial during the PETM [11, 12]. However, marine burial of terrestrial OC has received little attention, despite currently removing as much carbon per year (an estimated 41-75 megatons of carbon per year; MtC yr^{-1}) [13]) as silicate weathering and carbonate precipitation (an estimated 47−72 MtC yr^{-1}) [14].

Modern river data [15, 16] and lake sediments [17] suggest that the erosional flux of terrestrial OC is closely linked to hydroclimate. This implies that marine burial of terrestrial OC is a negative carbon cycle feedback that could operate during the PETM alongside silicate weathering [9] and marine organic carbon burial [11, 12]. However, marine burial of terrestrial OC has been interpreted to either increase [18] or decrease [19] during the PETM. This contradictory evidence suggests limitation with the current methodologies that we use to fingerprint terrestrial OC in marine sediments. Two-endmember mixing models are frequently used to reconstruct the proportion of terrestrial versus marine organic carbon in marine sediments (e.g., [19]) and assumes that all terrestrial OC is a single homogenous pool. However, terrestrial OC is demonstrably a heterogenous mixture of plant and soil OC [20], and mixing models that fail to distinguish between these two pools underestimate modern terrestrial OC burial in marine sediments by 40–85 % [21].

In this study, we employ a novel data-modelling approach to resolve these challenges and evaluate the role of the terrestrial OC cycle as a negative climate feedback during transient warming events. We trace the source-to-sink delivery of plant and soil OC from land to sea by compiling and generating new source-specific biomarker records from shallow marine PETM sites in New Jersey Margin, Tanzania, Denmark, the Tasman Sea, and the High Arctic. We use a three-endmember mixing model to apportion the sedimentary OC pool into soil, plant and marine OC, overcoming the challenges with previous estimates. These data are combined with measurements of total organic carbon, dry bulk density, and sedimentation rates, to quantify plant and soil OC burial fluxes in marine sediments during the PETM. We use fully-coupled paleoclimate models to assess the mechanisms responsible for changes in terrestrial OC export and re-assess the role of terrestrial OC burial in driving the long-term recovery of the Earth system following transient warming.

Coastal marine sediments dominated by terrestrial organic matter

The relative abundance of lipid biomarkers reveals distinct spatial and temporal patterns in organic matter provenance before, during and after the PETM. We use the terrestrial-aquatic ratio (TAR) to evaluate the relative abundance of short-vs-long-chain *n*-alkanes [22]. Short-chain *n*-alkanes are largely derived from algae/zooplankton (i.e. marine OC) whereas long-chain *n*-alkanes are derived from higher plants (i.e. plant OC) – the latter can be delivered into the marine realm via atmospheric transport (i.e. leaf abrasion) and/or via the erosion of catchments soils [22]. Values near 1 are associated with

delivery of higher plants into the marine realm, whereas values approaching 0 reflect greater input from algae or zooplankton. Each site in our compilation is characterised by TAR values > 0.7, indicating that plant OC is an important contributor to the marine sedimentary OC pool during the latest Palaeocene, PETM, and earliest Eocene.

We additionally use the branched-to-isoprenoid tetraether (BIT) index [23] to evaluate the relative abundance of branched glycerol dialkyl glycerol tetraethers (GDGTs) vs crenarchaeol. Branched GDGTs are derived from soil bacteria (i.e. soil OC) whereas crenarchaeol is derived from planktic ammonia-oxidising *Nitrososphaerota* (i.e. marine OC). BIT values approaching 1 are associated with the delivery of soil OC into the marine realm, whereas lower values reflect greater OC input from marine organisms. Prior to the PETM, BIT indices span a wide range and indicate: (i) a mixture of soil and marine OC burial in the High Arctic (BIT average: 0.42) and Denmark (BIT average: 0.56) and (ii) predominantly marine OC burial in the New Jersey Margin (average: 0.19) and Tasman Sea (average: 0.14). During the PETM, BIT indices decrease (Denmark, High Arctic, New Jersey Margin) [5, 24, 25] or remain stable (Tasman Sea) [26]. BIT values are only available for Tanzania during the PETM and suggest predominantly soil OC burial.

Using a three endmember mixing model (*Methods*), we apportion the sedimentary OC pool into soil, plant and marine OC. We find that coastal marine sediments are dominated by plant OC during the latest Palaeocene, PETM, and early Eocene (up to 90 % of the total [i.e. plant + soil + marine] OC pool) with a limited contribution from soil (typically ~5 to 15 %) and marine OC (typically ~5 to 20 %; Fig. 1; Extended Data Fig. 1-5). The relative proportion of soil vs. plant vs. marine OC in shallow marine sediments does not change dramatically (i.e. < 10%) between the latest Palaeocene and PETM (Fig. 1; Extended Data Fig. 1-5), except for Denmark, where the relative proportion of marine OC increases from ~34 to 61% (Extended Data Fig. 4). The higher proportion of marine OC in Denmark is attributed to localised volcanic ash deposition following eruptions within the North Atlantic Igneous Province and a resulting increase in marine primary productivity [27].

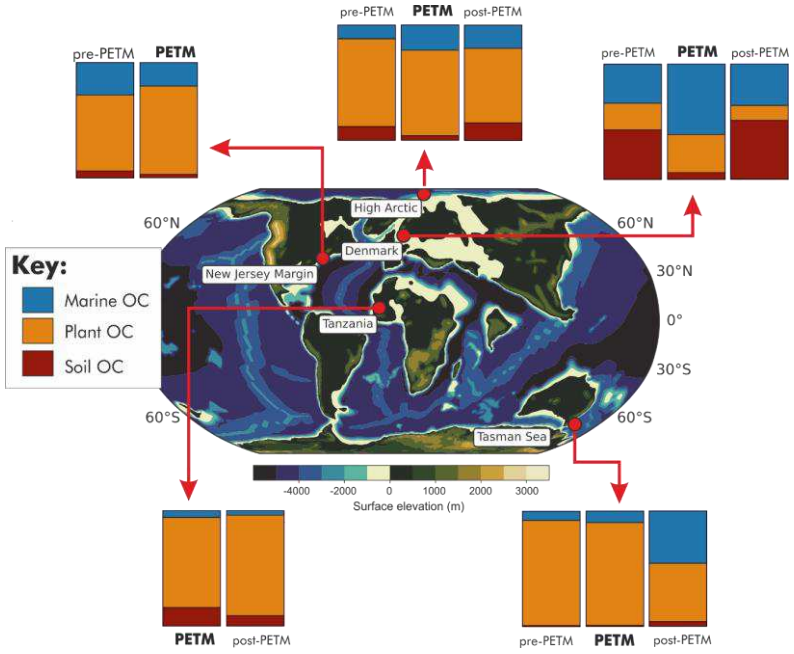

Figure 1: Organic matter distribution in coastal marine sediments during the Palaeocene-Eocene. Relative proportion of plant, soil and marine organic carbon (OC) in coastal marine sediments during the latest Palaeocene, PETM (onset, body, and recovery combined) and/or early Eocene. Data overlain upon early Eocene paleogeography (55 Ma) via ref. [28].

After accounting for differences in OC content, dry bulk density and sedimentation rates (*see Methods*), we show that between the latest Palaeocene and PETM, plant OC burial flux in marine sediments increased in the High Arctic (1.7-fold change; Fig. 2a) and the New Jersey Margin (13.3-fold change; Fig. 2a) and decreased slightly in the Tasman Sea (0.8-fold change; Fig. 2a). Soil OC burial flux in marine sediments increased in the New Jersey Margin (3.8-fold change; Fig. 2a) and decreased in the Tasman Sea (0.4-fold change; Fig. 2a) the High Arctic (0.5-fold change; Fig. 2a). Sedimentation rates in Denmark during the latest Palaeocene are uncertain [27] but there is a dramatic increase in plant OC burial flux (~50-fold change) and soil OC burial flux (~3-fold change) between the onset and body of the PETM – as pre-PETM sedimentation rates are unlikely to be higher than the PETM onset [29], we assume that this increase is representative of the PETM (Fig. 2a).

Two sites (New Jersey Margin, High Arctic) have sufficient proxy with suitable age control to evaluate how plant and soil OC burial flux evolved during the 'core' and 'recovery' of the PETM (defined following ref. [30, 31]). In the High Arctic (Fig. 2b) and New Jersey Margin (Fig 2c), plant and soil OC burial flux combined increased 2.6-fold and 1.3-fold between the 'body' and 'recovery' phase of the PETM, respectively.

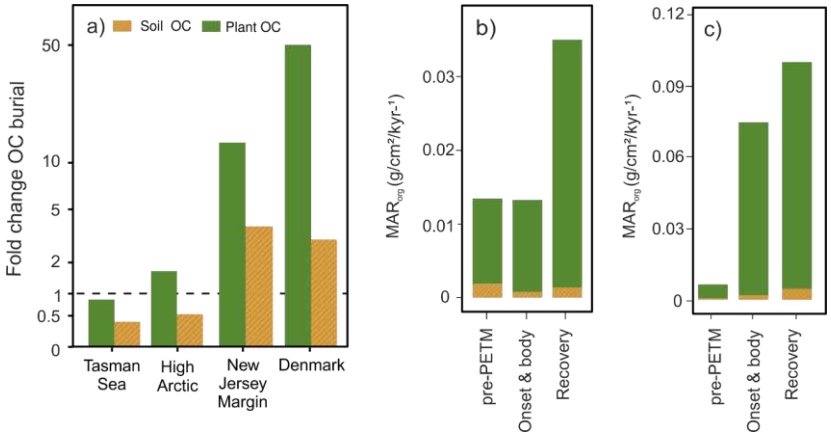

Figure 2: Plant and soil OC burial fluxes in coastal marine sediments during the Palaeocene-Eocene. (a) Fold change in plant OC (green solid bar) and soil OC burial (orange striped bar) in marine sediments during the PETM inferred via source-specific biomarker records. Y-axis is a pseudo-log scale. Values > 1 indicate higher OC burial. Values < 1 indicate lower OC burial. (b-c) Plant and soil OC MARs increase in (b) the High Arctic and (c) New Jersey Margin during the PETM recovery.

Overall, our results show that latest Palaeocene and PETM-aged coastal marine sediments are dominated by plant and soil OC, which contribute ca. 40 to >95 % of the total OC pool (Fig. 1). This is higher than observed in modern continental margin sediments (12-20 %) [32] but similar to modern deltaic sediments (43-91 %) [32] with high terrestrial OC burial efficiency (typically >25 % but up to 80 % in SE Asia and the High Arctic [33, 34]).

Hydroclimate modulates terrestrial organic carbon export

Hydroclimate can impact terrestrial OC export in two ways. First, it can control net primary productivity and soil carbon cycle processes, setting the available plant and soil OC in the landscape available for erosion [35]. Second, it impacts hydrological-driven erosion processes, which include a range of mass-wasting and runoff-driven processes that can mobilise terrestrial OC and transport it in river systems [16]. To assess how hydroclimate regulates the erosional export and subsequent burial of terrestrial OC in marine sediments, we use the Deep-Time Model Intercomparison Project (DeepMIP) suite of early Eocene model simulations [36] to simulate the impact of higher CO_2 on mean annual precipitation (MAP) at each site (*Methods*). The impact of higher CO_2 on MAP is regionally variable and either increases (Tasman Sea, High Arctic; New Jersey Margin; Denmark; Fig. 3) or decreases (Tanzania; Fig. 3). Tanzania is the only site that exhibits lower MAP estimates under elevated CO_2. However, high resolution climate model simulations [37] indicate more frequent extreme weather events at site. As extreme rainfall events help to mobilise terrestrial OC in modern settings [38], they likely regulate the erosional export of terrestrial OC at Tanzania.

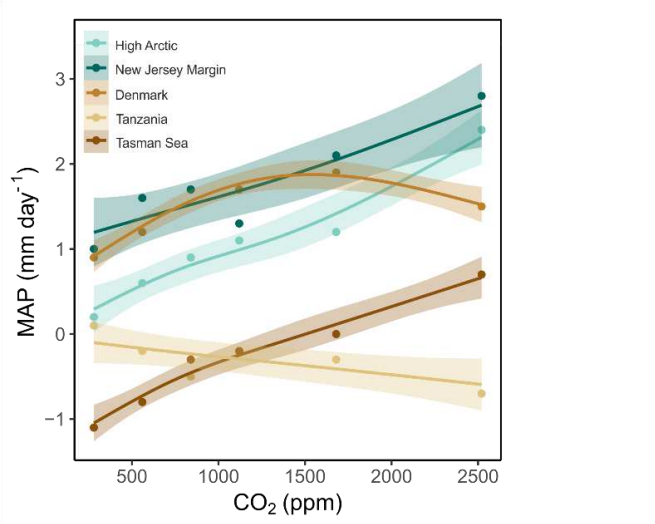

Figure 3: Relationship between atmospheric CO_2 and mean annual precipitation in early Eocene climate model simulations for various localities. Each data point represents the multi-model mean from the DeepMIP model ensemble [36] relative to a pre-industrial x1 CO_2 simulation. Colours refer to individual sites in our proxy compilation. Each site is fitted with a cubic regression spline (95% confidence intervals).

Higher temperatures and an enhanced hydrological cycle will affect plant and soil OC stocks and potentially, the relative proportion of soil OC versus plant OC transported from land to sea. Global- and regional-scale changes in plant and soil OC are assessed using a fully coupled atmosphere-ocean-vegetation model (HadCM3BL-M2.1Da; [39]; Fig. 4) with dynamic vegetation and terrestrial carbon cycle scheme (*Methods*). The terrestrial biosphere (i.e. plant and soil OC stocks combined; ~2,220 PgC) increases by ~6 % (150 PgC) between the latest Palaeocene (x2 pre-industrial (PI) CO_2) and PETM (x4 PI CO_2; Fig. 4e). This increase is notable but is modest compared to the mass of carbon thought to be released during the PETM (~3,000 to > 10,000 PgC) [40]. Our estimates are also much lower than the previously inferred increase in the terrestrial biosphere during the PETM inferred using stable carbon isotopes (2,000 PgC) [41], suggesting that the terrestrial biosphere only acts as a transient sink for excess carbon release. It also implies that changes in the size of OC stocks in the terrestrial biosphere cannot be the only driver of change.

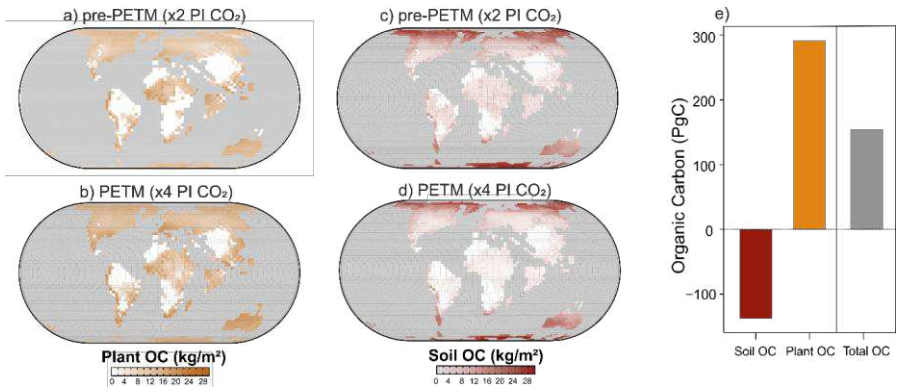

Figure 4: **Soil and plant OC stocks on land during the Palaeocene-Eocene inferred via an atmosphere-ocean-vegetation model**. Plant OC (a-b) and soil OC (c-d) stocks during the latest Palaeocene (x2 PI CO_2) and PETM (x4 PI CO_2) inferred via HadCM3BL-M2.1Da. (e) Difference in soil (red bar), plant (orange bar) and total terrestrial OC stocks (grey bar) between the latest Palaeocene (x2 PI CO_2) and PETM (x4 PI CO_2) simulations.

166 Latest Palaeocene and PETM-aged marine sediments show a high proportion of plant OC compared
167 to soil OC (Fig. 1), which contrasts with many modern-day river systems with high OC export that are
168 instead dominated by soil-derived OC [20]. This may suggest a smaller soil OC pool in past warm
169 climates, consistent with our simulated decline in global soil OC stocks under elevated CO_2 (Fig. 4c-d)
170 and empirical evidence for enhanced soil OC oxidation in mid-latitude interiors during the PETM [42,
171 43].
172
173 **Erosion rates are the primary driver of terrestrial carbon export**

174 Terrestrial OC burial rates are shown to increase by up to ~10-to-50 fold during the PETM (Fig. 2a) and
175 thus, cannot be explained solely by higher terrestrial primary productivity and a larger terrestrial
176 biosphere, as this change is relatively small (+6% relative to latest Palaeocene; Fig. 4e). This is
177 consistent with a comprehensive database of over forty modern river catchments showing that terrestrial
178 export of soil and plant-derived OC is largely insensitive to the magnitude of terrestrial primary
179 production [44]. Instead, the primary driver of terrestrial OC export in contemporary environments is the
180 capacity to supply and transport it in river sediment loads (i.e. physical erosion rates) [44].

181 The scaling of terrestrial OC export with erosion is important because it sets sedimentary accumulation
182 rates and OC burial efficiency [13]. This is apparent in modern large, erosive river catchments (e.g.,
183 Ganges–Brahmaputra rivers fed by the Himalaya erosional system) where high rates of sediment
184 delivery drives rapid accumulation offshore (burial efficiency in the Bay of Bengal approaches ~100 %;
185 [45]). It is also true of small mountainous rivers (e.g., Taiwan), where short transport lengths and very
186 high turbidity drive rapid sediment delivery to deeper water and burial efficiency are > 70 % [46]. As the
187 PETM is characterised by high erosional fluxes [29], high sedimentation rates [29] and low oxygen
188 availability [12, 29], these factors together likely explain why PETM sediments are characterised by
189 locally high plant and soil OC burial fluxes (Fig. 2).

190 **Organic carbon burial in past warm climates previously underestimated**

191 Erosion and subsequent burial of terrestrial OC in marine sediments could play a key role in modulating
192 PETM climate. However, widely used biogeochemical models [47] do not account for input and burial
193 of terrestrial OC in marine sediments. As such, the global significance of our findings remains uncertain.
194 Previous studies using organic carbon mass accumulation rates [12] suggest that between 40 to 86

MtC yr^{-1} of OC is sequestered in marine sediments during the PETM (assuming a duration of 270 kyr [12]) (see *Supplementary Information*). This occurs largely in coastal environments and restricted seaways [12] where the delivery of terrestrial OC is also likely to be high. If we assume that the relative proportion of terrestrial OC in PETM-aged marine sediments ranges between 40 to 95 % (Fig. 1), this implies that up to 81 MtC yr^{-1} of sedimentary marine OC in PETM-aged sediments is sourced from the terrestrial biosphere. This is comparable to the modern-day burial flux in marine sediments (41-75 MtC $yr^{-1;}$ [10]) and demonstrates the powerful role that the terrestrial carbon cycle could play during the PETM, including during the recovery phase (Fig. 2b-c).

This work offers tantalizing implications for other periods. Of particular relevance are the early Eocene hyperthermals (e.g., ETM2, H2) [2]. These share similar characteristics to the PETM, with evidence for global warming and enhanced physical erosion rates [48]. As these hyperthermals are relatively brief (typical duration ~100 kyr), they require the existence of a negative feedback mechanism that can operate over geologically short ($<10^4$ year) timescales. We suggest that terrestrial OC burial in marine sediments could explain the decline in global temperature after successive Eocene hyperthermals. It is also likely that terrestrial OC burial in marine sediments increased during other hyperthermals characterised by large changes in physical erosion rates, including the Permo-Triassic boundary (251.9 Ma; [49]), thus implying this feedback may be important throughout the Phanerozoic. Anthropogenic perturbations have also increased the flux of terrestrial OC carbon from land-to-sea [50], implying that marine burial of terrestrial OC could potentially aid the long-term (10^3 to 10^4 year) recovery of the Earth system after anthropogenic CO_2 emissions have ceased [1].

Methods

Biomarker analysis and data compilation

BIT indices were compiled from the following PETM-aged sites: (i) Tanzania (TDP Site 14) [29], (ii) New Jersey Margin (Ancora, Site 174AX) [5], (iii) Denmark (Fur) [25], (iv) Tasman Sea (ODP Site 1172) [26] and (v) the High Arctic (ACEX, IODP Site 302) [24]. Terrestrial-to-aquatic ratios (TARs) were compiled from (i) Tanzania (TDP Site 14) [29] and (ii) Denmark (Fur) [25]. To complement our data compilation, the terrestrial-to-aquatic ratio (TAR) was determined for PETM-aged sites in the: i) High Arctic (n = 94), (ii) Tasman Sea (n = 41), and (iii) New Jersey Margin (n = 42).

Sediments from the High Arctic, Tasman Sea and the New Jersey Margin were freeze dried, homogenized, and extracted using a MARS5 microwave-assisted extraction system (see ref. 5) using (i) DCM:MeOH (1:1, *v*:*v*); (ii) DCM:MeOH (9:1, *v*:*v*); and (iii) DCM. Solvents were heated for 30 minutes to 100 °C, followed by a hold time of 20 minutes. The extracts were subsequently combined into a total lipid extract (TLE) and separated into five fractions (see ref. [5] for more details). Hydrocarbon fractions (containing *n*-alkanes) were analysed using a ThermoFisher Trace 1310 Gas Chromatograph coupled to a Thermo TSQ8000 Triple Quadrupole MS (GC-MS/MS) at the University of Southamtpon. Separation was achieved with DB-5 column (30 m x 0.25 mm i.d, 0.25 µm film thickness). The GC-MS temperature program started at 70 °C for 1 minute, increased to 130 °C at 20 °C min^{-1}, followed by 300 °C at 4 °C min^{-1}, which was then held for 20 minutes. MS scanning occurred between mass-to-charge ratio (*m*/*z*) 50 to 650 Daltons, and an ionisation energy of 70 eV.

Biomarker proxies and endmember definitions

The branched-to-isoprenoid tetraether (BIT) [23] is defined as follows:

BIT = brGDGT-Ia + brGDGT-IIa + brGDGT-IIa' + brGDGT-IIIa + brGDGT-IIIa' / brGDGT-Ia + brGDGT-IIa + brGDGT-IIa' + brGDGT-IIIa + brGDGT-IIIa' + Crenarchaeol **[Eq. 1]**

The soil end-member for the BIT index was determined by compiling values in modern peat and soil environments (0.60-1.00; 95 % confidence intervals; n = 741) [51-61]. The marine end-member was defined using modern distal marine sediments (0.01-0.07; 95 % confidence intervals; n = 38) [55].

The terrestrial-to-aquatic ratio (TAR) is defined as follows:

$$TAR = C_{29} + C_{31} + C_{33} / (C_{17} + C_{19} + C_{21} + C_{29} + C_{31} + C_{33}) \quad \textbf{[Eq. 2]}$$

The plant end-member for the TAR was determined by compiling values in modern gymnosperms and angiosperms (0.83-1.00; 95 % confidence intervals; n = 1734) [62]. As there is no evidence that algae synthesise long-chain *n*-alkanes [63, 64], the marine end-member for the TAR was defined as 0.

Three endmember mixing model

The contributions of n end-members to a bulk sample can be constrained using $n - 1$ conservative tracers, plus the "sum-to-unity" constraint,

$$\sum_{j=1}^{n} \mathrm{f}j = 1, \qquad \textbf{[Eq. 3]}$$

where f_j is the fractional contribution of end-member j and $j \in 1 \ldots n$. This type of endmember mixing problem is classically written in matrix form as:

$$\begin{bmatrix} a_{1,1} & a_{1,2} & \cdots & a_{1,n} \\ \vdots & \vdots & \ddots & \vdots \\ a_{n-1,1} & a_{n-1,2} & \cdots & a_{n-1,n} \\ 1 & 1 & & 1 \end{bmatrix} \begin{bmatrix} f_1 \\ \vdots \\ f_{n-1} \\ f_n \end{bmatrix} = \begin{bmatrix} b_1 \\ \vdots \\ b_{n-1} \\ 1 \end{bmatrix} \qquad \textbf{[Eq. 4]}$$

where $a_{i,j}$ is the composition of conservative tracer i that describes end-member j—for example, the BIT value of the soil end-member or the TAR ratio of the plant end-member—and b_i is the measured value of conservative tracer i in a given sample. This is written more concisely as:

$$\boldsymbol{Af = b}, \qquad \textbf{[Eq. 5]}$$

where $\boldsymbol{A}$ is the $n \times n$ "design matrix", $\boldsymbol{f}$ is the $n \times 1$ vector of fractional abundances, and $\boldsymbol{b}$ is the $n \times 1$ vector of measured tracer values. This approach can be expanded to solve for f_i values of several samples simultaneously, assuming endmembers for all samples are described by the same design matrix, as

$$\boldsymbol{AF = B}, \qquad \textbf{[Eq. 6]}$$

where

$$\boldsymbol{F} = [\boldsymbol{f_1} \quad \boldsymbol{f_2} \quad \ldots \quad \boldsymbol{f_m}] \qquad \textbf{[Eq. 7]}$$

is the $n \times m$ matrix of fractional contributions,

$$\boldsymbol{B} = [\boldsymbol{b_1} \quad \boldsymbol{b_2} \quad \ldots \quad \boldsymbol{b_m}] \qquad \textbf{[Eq. 8]}$$

is the $n \times m$ matrix of measured tracer values, and m is the number of samples.

Assuming all $a_{i,j}$ and $b_{i,k}$ (where $k \in 1 \ldots m$) values are known perfectly, $\boldsymbol{F}$ can be solved by simply multiplying $\boldsymbol{B}$ by $\boldsymbol{A}^{-1}$, the inverse of $\boldsymbol{A}$. In practice, this is instead solved using a non-negative least-squares approach, as the inversion approach is highly sensitive to noise. However, we first describe a method of overcoming the fact that some conservative tracers only inform the relative contributions of a subset of end-members.

Some conservative tracers used here are insensitive to the fractional contributions of some end-members. For example, the BIT index is treated as a linear mixture of f_{soil} and f_{marine} only; it is insensitive to f_{plant} values. This can be seen mathematically as

$$BIT_{measured} = BIT_{soil}\left(\frac{f\text{soil}}{f\text{soil} + f\text{marine}}\right) + BIT_{algal}\left(\frac{f\text{marine}}{f\text{soil} + f\text{marine}}\right). \qquad \textbf{[Eq. 9]}$$

We must modify our model (Eqs. 4-6) accordingly to deal with this fact. Specifically, Eq. 9 can be re-written as

$$f_{\text{soil}}(BIT_{soil} - BIT_{measured}) + f_{\text{algal}}(BIT_{\text{marine}} - BIT_{measured}) = 0 \qquad \textbf{[Eq. 10]}$$

which is now a linear equation of f_i values. Similarly subtracting all measured results from end-member values, we re-write Eq. 4 as

$$\begin{bmatrix} (a_{1,1}-b_1) & (a_{1,2}-b_1) & \cdots & (a_{1,n}-b_1) \\ \vdots & \vdots & \ddots & \vdots \\ (a_{n-1,1}-b_{n-1}) & (a_{n-1,2}-b_{n-1}) & \cdots & (a_{n-1,n}-b_{n-1}) \\ 1 & 1 & \ldots & 1 \end{bmatrix} \begin{bmatrix} f_1 \\ \vdots \\ f_{n-1} \\ f_n \end{bmatrix} = \begin{bmatrix} 0 \\ \vdots \\ 0 \\ 1 \end{bmatrix} \quad \textbf{[Eq. 11]}$$

where any $(a_{i,j} - b_i)$ entry is set to zero if tracer i is insensitive to end-member j (e.g., $BIT_{plant} - BIT_{measured} \equiv 0$ since BIT_{plant} does not exist). This can similarly be written more concisely as

$$\boldsymbol{Xf} = \boldsymbol{z}; \quad \textbf{[Eq. 12]}$$

where $\boldsymbol{X} = \boldsymbol{A} - \boldsymbol{b}$ (with the exception of the final row, which remains all ones for the sum-to-unity constraint) and $\boldsymbol{z} = [\mathbf{0}1]^T$ is a vector of length n of all zeros except for the final entry. This can again be expanded to solve for $\boldsymbol{f}_i$ values of several samples simultaneously as

$$\begin{bmatrix} X_1 & 0 & \cdots & 0 \\ 0 & X_2 & \cdots & 0 \\ \vdots & \vdots & \ddots & \vdots \\ 0 & 0 & \cdots & X_m \end{bmatrix} \begin{bmatrix} f_1 \\ f_2 \\ \vdots \\ f_m \end{bmatrix} = \begin{bmatrix} z \\ z \\ \vdots \\ z \end{bmatrix} \quad \textbf{[Eq.13]}$$

Finally, we write this more concisely as

$$\boldsymbol{Y\varphi} = \boldsymbol{\zeta}, \quad \textbf{[Eq. 14]}$$

where $\boldsymbol{Y}$ is an $(n \times m) \times (n \times m)$ diagonal block design matrix, $\boldsymbol{\varphi}$ is a matrix of size $n \times m$ containing all fractional contributions, and $\boldsymbol{\zeta}$ is a matrix of size $n \times m$ containing m entries of $\boldsymbol{z}$. Eq. 14 describes our model. Rather than solving directly by inverting $\boldsymbol{Y}$—which is highly sensitive to analytical noise and end- member uncertainty, as described above—we solve Eq. 14 using a non-negative least squares approach. Specifically, we find the vector $\boldsymbol{\varphi}$ that satisfies

$$\min_{\boldsymbol{\varphi}} \|\boldsymbol{\zeta} - \boldsymbol{Y\varphi}\| \quad \textbf{[Eq. 15]}$$

subject to the constraint

328

329 $$\boldsymbol{\varphi}_l \geq 0, \quad l = 1, \ldots, n \times m \qquad \textbf{[Eq. 16]}$$

330

331 using the non-negative least squares algorithm as implemented in the SciPy package for Python. Eq.
332 15-16 describe the model solution that minimizes the norm of the residual error (i.e., the RMSE, root
333 mean square error) while fulfilling the constraints that each $\boldsymbol{f}_k$ is non-negative and sums to unity.

334 To account for uncertainty in prescribed end-member compositions—as well as in the sum-to-unity
335 constraint—and to estimate uncertainty on each calculated fractional contribution, we solve our model
336 in a Monte Carlo fashion. Specifically, we draw each $a_{i,j}$ value from a uniform distribution that
337 encompasses the 90% confidence interval of all measured values for a particular tracer of a particular
338 end-member. We additionally slightly relax the sum-to-unity constraint by adding random error, E, to
339 each entry of the final row of each X_k design matrix. This approach allows for, e.g., small contributions
340 by an additional, unidentified end-member. Specifically, here we allow for 5 % error (i.e., $E \in (-0.05,$
341 $0.05)$) drawn uniformly. We then solve Eqs. 15-16 and repeat this process 100,000 times.

342 Ideally, Eqs. 15-16 will yield a perfect solution (i.e., RMSE = 0) for the case of *n* end-members and n
343 − 1 conservative tracers. However, if measured values are outside of the prescribed end-member
344 range (e.g., if $BIT_{measured} > BIT_{soil}$), then RMSE will be greater than zero. We therefore only retain the
345 1 % of solutions (i.e., 1,000 iterations) that yield the lowest RMSE values for all samples. In addition
346 to providing an estimate of uncertainty on end-member contributions, this approach also allows us to
347 estimate which range of measured end-member compositions best describes a given sample set.

348

349 *Plant, soil, and marine-derived OC mass accumulation rates during the PETM*

350 Mass accumulation rates of plant, soil, and marine OC (MARs; in g cm^{-2} kyr^{-1}) are calculated for the
351 latest Palaeocene and PETM using linear sedimentation rates (LSR; cm kyr^{-1}), dry bulk density (ρ; g
352 cm^{-3}) [65], OC measurements, and the proportion of plant, soil, or marine OC (f_x) inferred via a three
353 end-member mixing model calculated using Eq. 17:

354

$$MAR = LSR * \rho * (TOC / 100) * f_x \quad \textbf{[Eq. 17]}$$

Commented [EHH1]: TOC?

where LSR is linear sedimentation rate (cm kyr^{-1}), ρ is dry bulk density (g cm^{-3}) [65], TOC is total organic carbon concentrations (wt. %) and f_x is the proportion of plant, soil, or marine OC (f_x) inferred via a three end-member mixing model as described above. Linear sedimentation rates for the High Arctic, Tasman Sea, Tanzania, New Jersey Margin and Denmark, are obtained via ref. [27, 30, 31] (see Supplementary Information). Linear sedimentation rates for Denmark are well constrained during the onset (2.2 cm/kyr^{-1}), body (23.8cm/kyr^{-1}) and recovery (2.8 cm/kyr^{-1}) of the PETM [27] but uncertain prior to the PETM onset. As pre-PETM sedimentation rates are unlikely to be higher than sedimentation rates during the PETM onset [29], we assume a value of 2.2 cm/kyr^{-1}. TOC estimates are obtained via ref. [30] and. ref. [25]. Published bulk density values are only available for one site (Tasman Sea), and thus a constant ρ value of 2.65 g/cm^{-3} was assumed across all the sites following ref. [66].

Climate modelling experiments

We use the DeepMIP ensemble of model simulations, part of Phase 4 of the Paleoclimate Modelling Intercomparison Project (PMIP4) [67] and integrated within CMIP6 (Coupled Model Intercomparison Project Phase 6; [68]). The experimental design is detailed in [69], with an overview of large-scale climate features provided by [36]. Simulations have been run at different atmospheric CO_2 levels—typically ×1, ×3, ×6, and ×9 preindustrial (PI) CO_2, but with a subset of these, or additional atmospheric CO_2 concentrations, chosen by some model groups [36]. Simulations have been performed with eight different models and detailed descriptions of the models and simulations are provided in [36]. The analysed climatologies (land air temperature, mean annual precipitation) are based on the last 100 years of each simulation. MAP was extracted from each simulation and normalised relative to the pre-industrial x1 CO_2 simulation with modern geography to remove the effect of non-CO_2 boundary conditions.

The Hadley Centre model was used to quantify plant and soil OC stocks under two different CO_2 levels (x2 and x4 PI CO_2). This model uses the MOSES2.1 land scheme and has a dynamic vegetation and terrestrial carbon cycle scheme, TRIFFID (Top-down Representation of Interactive Foliage and Flora including Dynamics) [35, 39]. The exact model configuration (HadCM3BL-M2.1Da) is described in detail

in [39]. Two simulations were performed: (i) a late Palaeocene simulation with atmospheric CO_2 concentrations of 560 ppmv and (ii) a PETM simulation with atmospheric CO_2 concentrations of 1,120 ppmv [70]. Both simulations use time-dependant boundary conditions (land-sea mask, bathymetry, topography (Getech Plc) and solar luminosity (1354.98 W/m^2). Climate means are produced from the last 100 years. Each simulation is run for over 8,000 model years to ensure they are fully equilibrated in the atmosphere, land and deep ocean.

Acknowledgements

GNI acknowledges funding from Royal Society Dorothy Hodgkin Fellowship grant DHF/R1/191178, RF/ERE/231019, and RF/ERE/210068. EH acknowledges funding from a NERC PhD studentship (NE/S007210). FE acknowledges funding from the Deutsche Forschungsgemeinschaft (441217575 and 527682349). AF and PJV acknowledge funding from NERC grants NE/V011405/1 & NE/X015505/1. MB acknowledge funding from NERC grant NE/J008591/. TMG acknowledges support from the WoodNext Foundation, a donor-advised fund. We thank Sargent Bray at the University of Southampton, Katiana Doeana and Susan Carter at Havard University, and the NERC Life Sciences Mass Spectrometry Facility (now the National Environmental Isotope Facility) for technical support and assistance. For TDP Site 14 samples, we thank colleagues in the Tanzanian Drilling Project, and especially those from the Tanzanian Petroleum Development Corporation. This research also used samples provided by the Ocean Drilling Program (ODP) and the International Ocean Drilling Program (IODP).

Author Contributions

G.N.I designed the research and wrote the manuscript. Mixing model developed by J.H. Samples collected and/or analysed by E.H, F.J.E., M.P.S.B, R.D.P and A.P. Climate simulations provided by R.S, P.V and A.F. All authors reviewed and edited the final version of the paper.

Data availability

All data used and source data for figures and tables in this study are available via figshare at [reference to be added]. Source data are provided with this paper.

Ethics declarations

The authors declare no competing interests.

Source data

Source data for Fig. 1-4 and Extended Data Figures 1-5 are included in the supplementary information.

References

1. Tierney, J.E., et al., *Past climates inform our future.* science, 2020. **370**(6517): p. eaay3701.
2. Harper, D.T., et al., *Long-and short-term coupling of sea surface temperature and atmospheric CO2 during the late Paleocene and early Eocene.* Proceedings of the National Academy of Sciences, 2024. **121**(36): p. e2318779121.
3. McInerney, F.A. and S.L. Wing, *The Paleocene-Eocene Thermal Maximum: A perturbation of carbon cycle, climate, and biosphere with implications for the future.* Annual Review of Earth and Planetary Sciences, 2011. **39**(1): p. 489-516.
4. Inglis, G.N., et al., *Global mean surface temperature and climate sensitivity of the EECO, PETM and latest Paleocene.* Climate of the Past 2020. **2020**: p. 1-43.
5. Elling, F.J., et al., *Archaeal lipid biomarker constraints on the Paleocene-Eocene carbon isotope excursion.* Nature Communications, 2019. **10**(1): p. 4519.
6. Berner, R.A., *The long-term carbon cycle, fossil fuels and atmospheric composition.* Nature, 2003. **426**(6964): p. 323-326.
7. Merdith, A.S., et al., *Phanerozoic icehouse climates as the result of multiple solid-Earth cooling mechanisms.* Science Advances, 2025. **11**(7): p. eadm9798.
8. Walker, J.C., P. Hays, and J.F. Kasting, *A negative feedback mechanism for the long-term stabilization of Earth's surface temperature.* Journal of Geophysical Research: Oceans, 1981. **86**(C10): p. 9776-9782.
9. Pogge von Strandmann, P.A., et al., *Lithium isotope evidence for enhanced weathering and erosion during the Paleocene-Eocene Thermal Maximum.* Science Advances, 2021. **7**(42): p. eabh4224.
10. Walters, G.L., et al., *Clay hydroxyl isotopes show an enhanced hydrologic cycle during the Paleocene-Eocene Thermal Maximum.* Nature Communications, 2022. **13**(1): p. 7885.
11. Behrooz, L., et al., *North-East Peri-Tethyan Water Column Deoxygenation and Euxinia at the Paleocene Eocene Thermal Maximum.* Paleoceanography and Paleoclimatology, 2024. **39**(11): p. e2023PA004828.

12. Papadomanolaki, N.M., A. Sluijs, and C.P. Slomp, *Eutrophication and deoxygenation forcing of marginal marine organic carbon burial during the PETM.* Paleoceanography and Paleoclimatology, 2022. **37**(3): p. e2021PA004232.
13. Blair, N.E. and R.C. Aller, *The Fate of Terrestrial Organic Carbon in the Marine Environment.* Annual Review of Marine Science, 2012. **4**(Volume 4, 2012): p. 401-423.
14. Gaillardet, J., et al., *Global silicate weathering and CO2 consumption rates deduced from the chemistry of large rivers.* Chemical geology, 1999. **159**(1-4): p. 3-30.
15. Clark, K.E., et al., *Extreme rainstorms drive exceptional organic carbon export from forested humid-tropical rivers in Puerto Rico.* Nature communications, 2022. **13**(1): p. 2058.
16. Hilton, R.G., *Climate regulates the erosional carbon export from the terrestrial biosphere.* Geomorphology, 2017. **277**: p. 118-132.
17. Howarth, J.D., et al., *Long term carbon export from mountain forests driven by hydroclimate and extreme event driven landsliding.* Communications earth & environment, 2025. **6**(1): p. 432.
18. John, C.M., et al., *North American continental margin records of the Paleocene-Eocene thermal maximum: Implications for global carbon and hydrological cycling.* Paleoceanography, 2008. **23**(2).
19. Sluijs, A. and G.R. Dickens, *Assessing offsets between the δ13C of sedimentary components and the global exogenic carbon pool across early Paleogene carbon cycle perturbations.* Global Biogeochemical Cycles, 2012. **26**(4).
20. Hilton, R.G., M. Schwab, and V. Galy, *Dynamics of particulate organic carbon mobilization, storage, and export across river sedimentary systems*, in *Treatise on Geochemistry (Third edition)*, A. Anbar and D. Weis, Editors. 2025, Elsevier: Oxford. p. 215-250.
21. Gordon, E.S. and M.A. Goñi, *Sources and distribution of terrigenous organic matter delivered by the Atchafalaya River to sediments in the northern Gulf of Mexico.* Geochimica et Cosmochimica Acta, 2003. **67**(13): p. 2359-2375.
22. Pancost, R.D. and C.S. Boot, *The palaeoclimatic utility of terrestrial biomarkers in marine sediments.* Marine Chemistry, 2004. **92**(1-4): p. 239-261.
23. Hopmans, E.C., et al., *A novel proxy for terrestrial organic matter in sediments based on branched and isoprenoid tetraether lipids.* Earth and Planetary Science Letters, 2004. **224**(1-2): p. 107-116.

24. Sluijs, A., et al., *Late Paleocene–early Eocene Arctic Ocean sea surface temperatures: reassessing biomarker paleothermometry at Lomonosov Ridge.* Climate of the Past, 2020. **16**(6): p. 2381-2400.
25. Stokke, E.W., et al., *Temperature changes across the Paleocene-Eocene Thermal Maximum – a new high-resolution TEX86 temperature record from the Eastern North Sea Basin.* Earth and Planetary Science Letters, 2020. **544**: p. 116388.
26. Sluijs, A., et al., *Southern ocean warming, sea level and hydrological change during the Paleocene-Eocene thermal maximum.* Climate of the Past, 2011. **7**(1): p. 47-61.
27. Jones, M.T., et al., *Tracing North Atlantic volcanism and seaway connectivity across the Paleocene–Eocene Thermal Maximum (PETM).* Clim. Past, 2023. **19**(8): p. 1623-1652.
28. Steinig, S., et al., *DeepMIP-Eocene-p1: multi-model dataset and interactive web application for Eocene climate research.* Scientific Data, 2024. **11**(1): p. 970.
29. Carmichael, M.J., et al., *Hydrological and associated biogeochemical consequences of rapid global warming during the Paleocene-Eocene Thermal Maximum.* Global and Planetary Change, 2017. **157**: p. 114-138.
30. Hollingsworth, E.H., et al., *Spatial and Temporal patterns in petrogenic organic carbon Mobilization during the paleocene-Eocene thermal maximum.* Paleoceanography and Paleoclimatology, 2024. **39**(2): p. e2023PA004773.
31. Doubrawa, M., et al., *Shelf Ecosystems Along the U.S. Atlantic Coastal Plain Prior to and During the Paleocene-Eocene Thermal Maximum: Insights Into the Stratigraphic Architecture.* Paleoceanography and Paleoclimatology, 2022. **37**(10): p. e2022PA004475.
32. Burdige, D.J., *Burial of terrestrial organic matter in marine sediments: A re-assessment.* Global Biogeochemical Cycles, 2005. **19**(4).
33. Kim, D., et al., *Changes in the burial efficiency and composition of terrestrial organic carbon along the Mackenzie Trough in the Beaufort Sea.* Estuarine, Coastal and Shelf Science, 2022. **275**: p. 107997.
34. Yu, M., et al., *Persistently high efficiencies of terrestrial organic carbon burial in Chinese marginal sea sediments over the last 200 years.* Chemical Geology, 2022. **606**: p. 120999.
35. Cox, P.M., et al., *Acceleration of global warming due to carbon-cycle feedbacks in a coupled climate model.* Nature, 2000. **408**(6809): p. 184-187.

36. Lunt, D.J., et al., *DeepMIP: Model intercomparison of early Eocene climatic optimum (EECO) large-scale climate features and comparison with proxy data.* Climate of the Past, 2021. **17**(1): p. 203-227.
37. Carmichael, M.J., R.D. Pancost, and D.J. Lunt, *Changes in the occurrence of extreme precipitation events at the Paleocene–Eocene thermal maximum.* Earth and Planetary Science Letters, 2018. **501**: p. 24-36.
38. Hilton, R.G., et al., *Tropical-cyclone-driven erosion of the terrestrial biosphere from mountains.* Nature Geoscience, 2008. **1**(11): p. 759-762.
39. Valdes, P.J., et al., *The BRIDGE HadCM3 family of climate models: HadCM3@Bristol v1.0.* Geosci. Model Dev., 2017. **10**(10): p. 3715-3743.
40. Gutjahr, M., et al., *Very large release of mostly volcanic carbon during the Palaeocene–Eocene Thermal Maximum.* Nature, 2017. **548**(7669): p. 573-577.
41. Bowen, G.J. and J.C. Zachos, *Rapid carbon sequestration at the termination of the Palaeocene–Eocene Thermal Maximum.* Nature Geoscience, 2010. **3**(12): p. 866-869.
42. Baczynski, A.A., et al., *Distortion of carbon isotope excursion in bulk soil organic matter during the Paleocene-Eocene thermal maximum.* GSA Bulletin, 2016. **128**(9-10): p. 1352-1366.
43. Denis, E.H., et al., *Decreased soil carbon in a warming world: Degraded pyrogenic carbon during the Paleocene-Eocene Thermal Maximum, Bighorn Basin, Wyoming.* Earth and Planetary Science Letters, 2021. **566**: p. 116970.
44. Galy, V., B. Peucker-Ehrenbrink, and T. Eglinton, *Global carbon export from the terrestrial biosphere controlled by erosion.* Nature, 2015. **521**(7551): p. 204-207.
45. Galy, V., et al., *Efficient organic carbon burial in the Bengal fan sustained by the Himalayan erosional system.* Nature, 2007. **450**(7168): p. 407-410.
46. Kao, S.J., et al., *Preservation of terrestrial organic carbon in marine sediments offshore Taiwan: mountain building and atmospheric carbon dioxide sequestration.* Earth Surf. Dynam., 2014. **2**(1): p. 127-139.
47. Komar, N. and R.E. Zeebe, *Redox-controlled carbon and phosphorus burial: A mechanism for enhanced organic carbon sequestration during the PETM.* Earth and Planetary Science Letters, 2017. **479**: p. 71-82.

48. Rush, W., et al., *Assessing environmental change associated with early Eocene hyperthermals in the Atlantic Coastal Plain, USA.* Clim. Past, 2023. **19**(8): p. 1677-1698.
49. Sephton, M.A., et al., *Catastrophic soil erosion during the end-Permian biotic crisis.* Geology, 2005. **33**(12): p. 941-944.
50. Regnier, P., et al., *Anthropogenic perturbation of the carbon fluxes from land to ocean.* Nature geoscience, 2013. **6**(8): p. 597-607.
51. Naafs, B.D.A., et al., *Introducing global peat-specific temperature and pH calibrations based on brGDGT bacterial lipids.* Geochimica et Cosmochimica Acta, 2017. **208**: p. 285-301.
52. French, D.W., et al., *Spatial distributions of core and intact glycerol dialkyl glycerol tetraethers (GDGTs) in the Columbia River Basin and Willapa Bay, Washington: Insights into origin and implications for the BIT index.* Organic Geochemistry, 2015. **88**: p. 91-112.
53. De Jonge, C., et al., *Drastic changes in the distribution of branched tetraether lipids in suspended matter and sediments from the Yenisei River and Kara Sea (Siberia): Implications for the use of brGDGT-based proxies in coastal marine sediments.* Geochimica et Cosmochimica Acta, 2015. **165**: p. 200-225.
54. Li, J., et al., *Distribution of glycerol dialkyl glycerol tetraether (GDGT) lipids in a hypersaline lake system.* Organic Geochemistry, 2016. **99**: p. 113-124.
55. Weijers, J.W., et al., *Constraints on the sources of branched tetraether membrane lipids in distal marine sediments.* Organic Geochemistry, 2014. **72**: p. 14-22.
56. Naeher, S., et al., *Sources of glycerol dialkyl glycerol tetraethers (GDGTs) in catchment soils, water column and sediments of Lake Rotsee (Switzerland)–Implications for the application of GDGT-based proxies for lakes.* Organic geochemistry, 2014. **66**: p. 164-173.
57. Peaple, M.D., et al., *Identifying the drivers of GDGT distributions in alkaline soil profiles within the Serengeti ecosystem.* Organic Geochemistry, 2022. **169**: p. 104433.
58. Bertassoli Jr, D.J., et al., *Controls on the distributions of GDGTs and n-alkane isotopic compositions in sediments of the Amazon River Basin.* Chemical Geology, 2022. **594**: p. 120777.
59. Li, J., et al., *Depth related variation of isoprenoid and hydroxylated tetraether lipids in Lake Lugu, Southwest China: Implications for palaeoenvironmental reconstructions.* Chemical Geology, 2023. **619**: p. 121313.

60. Guo, J., et al., *Assessing branched tetraether lipids as tracers of soil organic carbon transport through the Carminowe Creek catchment (southwest England).* Biogeosciences, 2020. **17**(12): p. 3183-3201.
61. Wang, H., et al., *Biomarker-based quantitative constraints on maximal soil-derived brGDGTs in modern lake sediments.* Earth and Planetary Science Letters, 2023. **602**: p. 117947.
62. Bush, R.T. and F.A. McInerney, *Leaf wax n-alkane distributions in and across modern plants: implications for paleoecology and chemotaxonomy.* Geochimica et Cosmochimica Acta, 2013. **117**: p. 161-179.
63. Chevalier, N., et al., *Precise indices based on n-alkane distribution for quantifying sources of sedimentary organic matter in coastal systems.* Organic Geochemistry, 2015. **88**: p. 69-77.
64. Bourbonniere, R.A. and P.A. Meyers, *Sedimentary geolipid records of historical changes in the watersheds and productivities of Lakes Ontario and Erie.* Limnology and Oceanography, 1996. **41**(2): p. 352-359.
65. Dadey, K.A., T. Janecek, and A. Klaus, *37. Dry-bulk density: its use and determination.* Proceedings of the Ocean Driling Program, Scientific Results, 1992. **126**.
66. Lyons, S.L., et al., *Palaeocene–Eocene Thermal Maximum prolonged by fossil carbon oxidation.* Nature Geoscience, 2019. **12**(1): p. 54-60.
67. Kageyama, M., et al., *The PMIP4 contribution to CMIP6–Part 1: Overview and over-arching analysis plan.* Geoscientific Model Development, 2018. **11**(3): p. 1033-1057.
68. Eyring, V., et al., *Overview of the Coupled Model Intercomparison Project Phase 6 (CMIP6) experimental design and organization.* Geoscientific Model Development, 2016. **9**(5): p. 1937-1958.
69. Lunt, D.J., et al., *The DeepMIP contribution to PMIP4: Experimental design for model simulations of the EECO, PETM, and pre-PETM (version 1.0).* Geoscientific Model Development, 2017. **10**(2): p. 889-901.
70. Sarkar, S., et al., *Shallow water records of the PETM: novel Insights from NE India (Eastern Tethys).* Paleoceanography and Paleoclimatology, 2022. **37**(7): p. e2021PA004257.

Supplementary Files

This is a list of supplementary files associated with this preprint. Click to download.

- SourcedataInglis2025.xlsx
- SupplementaryFigures.pdf